Deformation stage identification in steel material using acoustic emission with a hybrid denoising method and artificial neural network

Cheng, Lu; Sun, Qingkun; Yan, Rui; Groves, Roger M.; Veljkovic, Milan

DOI
10.1016/j.ymssp.2024.111805

Publication date
2024

Document Version
Final published version

Published in
Mechanical Systems and Signal Processing

Mechanical Systems and Signal Processing 222 (2025) 111805

Contents lists available at ScienceDirect

Mechanical Systems and Signal Processing

journal homepage: www.elsevier.com/locate/ymssp

Deformation stage identification in steel material using acoustic emission with a hybrid denoising method and artificial neural network

Lu Cheng [a,*], Qingkun Sun [a], Rui Yan [a,c], Roger M. Groves [b], Milan Veljkovic [a]

[a] Department of Engineering Structures, Delft University of Technology, Delft, The Netherlands
[b] Faculty of Aerospace, Delft University of Technology, Delft, The Netherlands
[c] Department of Civil and Environmental Engineering, Hong Kong Polytechnic University, Hong Kong, China

ARTICLE INFO

Keywords:
Denoising method
Singular spectrum analysis (SSA)
Variational mode decomposition (VMD)
Artificial neural network
Deformation stage
Acoustic emission

ABSTRACT

Acoustic emission (AE) is widely used for identifying source mechanisms and the deformation stage of steel material. The effectiveness of this non-destructive monitoring technique heavily depends on the quality of the measured AE signals. However, the AE signals from deformation are easily contaminated by the signals from noise in a noisy environment. This paper presents a hybrid model for deformation stage identification, which combines a self-adaptive denoising technique and an Artificial neural network (ANN). In pursuit of model generality, AE signals were collected from tensile coupon tests with various steel materials and loading speeds. First, a decomposition-based denoising method is applied based on the singular spectral analysis (SSA) and variational mode decomposition (VMD), which is defined as SSA-VMD. Its effectiveness is demonstrated by simulated signals and experimental results. Following the use of the denoising technique, an ANN is constructed to identify the deformation stage of steel materials with the input of features extracted from the filtered AE signals. The results indicate that the ANN achieves a high prediction accuracy of 0.93 in the test set and 0.87 in unseen data. By applying this denoising method, the ANN-based approach enables accurate correlation of the collected AE signals to deformation stages. The finding can be used as the basis for the creation of new methodologies for monitoring structural health status of in-service steel structures.

1. Introduction

The macroscopic mechanical properties of steel structures degrades while in service, originating from void nucleation together with inelastic deformation [1]. Steel structures then collapse when significant deformation has accumulated. A substantial amount of study into the mechanical behaviour description and damage propagation of steel material over many years has contributed to their safe application [2–7]. In addition to applying destructive testing methods, it is also essential to identify and monitor the deformation status and fracture behaviour of steel materials utilizing non-destructive testing techniques [8,9].

A passive NDT technique, Acoustic emission (AE), has been extensively used in early damage detection and real-time assessment of steel structures [10–13]. AE signals are generated by suddenly released energy from deformation within a metal [14]. Dunegan et al.

* Corresponding author.
E-mail address: clsilence@outlook.com (L. Cheng).

https://doi.org/10.1016/j.ymssp.2024.111805
Received 4 February 2024; Received in revised form 22 July 2024; Accepted 1 August 2024

[15] first correlated the characteristics of collected AE signals to the fracture mechanisms of precipitated alloys, such as beryllium and aluminium. This research showed the potential of the AE technique for fracture analysis of metal materials. After that, systematic studies of AE signals generated during the tensile deformation of metal materials were conducted [16–20]. With the development of microstructural examination [21–23], the generation of AE signals during the deformation process have been explained using the underlying mechanisms in metals and alloys. It was concluded that AE signals are dominantly produced by dislocation activity in the micro- and macro-yielding zones of metals, as well as the final fracture.

The association between AE features and the deformation stage in metals has been established further. A range of AE features, such as amplitude, energy, counts, hits, and root-mean-square (RMS), have been successfully confirmed to interpret the rupture process of material [20,24–30]. Various novel indicators, including combined partial energy ratio (PER) and the weighted peak frequency (WPF) [31], and the ratio of signal energy across two frequency ranges [32], have been proposed to improve AE monitoring systems and data processing techniques. [31–34]. Although individual pattern of AE signals for metal material deformation can be obtained, the related quantitative description is not transferable among studies. This is mainly because the AE characteristics are influenced by several factors, such as types of material, plasticity level, presence of any inclusions, and the employed AE acquisition system [32]. In addition, it was also found that signals generated during plastic deformation have overlapped distribution of AE features to final fracture [35]. If monitoring is not initiated at the beginning, it is challenging to distinguish the signals from plastic deformation and fracture based just on certain or synthetic analyses of AE features. Hence, it is necessary to propose a generalized method to correlate the collected AE signals to deformation stages.

Machine learning (ML) methods have gained significant attention for material characterization [36–38], including *k*-nearest neighbours (KNNs), Support Vector Machines (SVM), Artificial Neural Networks (ANNs), classification tree. Among these methods, ANNs have been successfully employed to help to enhance the understanding of materials and their properties. Applications include the characterization of corrosion, fatigue, creep rupture, flow behaviour and work hardening, and tensile behaviour [38]. Comparative analyses of various ML approaches in several studies [39–41] have demonstrated that ANNs outperform other classifiers in classifying tensile properties. Consequently, researchers have widely utilized ANNs to detect deformation stages in steel materials subjected to static tensile loading [37,42].

The performance of the ANN method is highly dependent on the quality of the AE signals. Meanwhile, the collected AE signals are always accompanied by complex noise in practical cases (e.g. friction noise between components and equipment, background noise from the environment). AE signals resulting from metal deformation are typically nonlinear and non-stationary [43]. Signal decomposition methods were presented to decompose the nonstationary signals into several regular clear sub-signals, which can be effectively used to remove the noises of nonstationary signals. Representative methods include wavelet transform (WT) [44], empirical mode decomposition (EMD) [45], ensemble empirical mode decomposition (EEMD) [46], and variational mode decomposition (VMD) [47]. VMD outperforms EMD and WT in terms of theoretical foundation, anti-noise performance and alleviating the mode mixing problem [48]. Whereas, the user-defined decomposition mode numbers severely affect its reliability. Furthermore, Zhou [49] found that VMD cannot effectively isolate low-frequency random noise. To solve the abovementioned drawbacks, some studies [49–51] have introduced an enhanced VMD method combined with the singular spectral analysis (SSA) [52], called the VMD-SSA method [49–51]. This approach employs VMD to remove highly oscillatory parts, followed by the SSA to filter out residual low-frequency random wavenumbers. Natarajan [53] and Xiang [54] proposed the use of the SSA-VMD method to reduce high-frequency interference for wind speed forecasting. This two-stage decomposition model has been validated for its effectiveness in addressing non-stationary data. Given the non-stationary nature of AE signals, a hybrid model based on SSA-VMD method is proposed in this research to denoise AE signals to improve the performance of the signal processing step.

In this paper, we aimed to improve and explore the application of ANN-based deformation stage identification for steel material with less contaminated AE signals. This study stands as one of the initial attempts to utilize SSA-VMD as the denoising technique for AE signals. After verifying the performance of the proposed denoising method, measured AE signals were obtained via a series of coupon steel tensile tests. Moreover, to improve the generalization of the ANN model, the tests were conducted with various steel grades, different geometries of coupons, and different loading rates. An improved ANN is finally designed and employed for signal identification during tensile deformation.

This paper is organized as follows: Section 2 presents the applied SSA-VMD model. Section 3 demonstrates the performance of the two-stage denoising method using a simulated AE signal. The experimental program and results are described in Section 4. Finally, section 5 describes the employed ANN for signal identification with hyperparameter tuning. The conclusion is given in Section 6.

2. Denoising methodology

2.1. SSA-VMD

The SSA-VMD denoising approach is utilized to overcome common issues in selecting the proper parameters for SSA and VMD (number of rows of the Hankel matrix for SSA and decomposition level for VMD) [55,56]. Two basic assumptions are made: (1) signals are composed of several narrow-bandwidth signals; (2) the frequency of the noise is overlapping with that of the real AE signals, but the corresponding frequency peak is different. These two assumptions are theoretically accurate considering the nature of the signals. The idea behind this approach is that SSA can efficiently eliminate strong broadband noise, and VMD can accurately remove the narrowband noise. The full procedure is as follows:

Step 1: SSA.

SSA is a principal component analysis for time series and is widely used to extract qualitative dynamics from noise-contaminated

signals [52].

Step 1.1- Embedding: The one-dimensional AE signal $X = (x_1, \ldots, x_N)$ is converted to a 2D matrix Y, namely the Hankel matrix.

$$Y = \begin{pmatrix} x_1 & x_2 & \ldots & \ldots & x_K \\ x_2 & x_3 & \ldots & \ldots & x_{K+1} \\ . & . & \ldots & \ldots & . \\ . & . & \ldots & \ldots & . \\ x_L & x_{L+1} & \ldots & \ldots & x_N \end{pmatrix} \tag{1}$$

where L is the number of rows ($1 < L < N$) and K is defined as N-L+1. Xu et al. [55] concluded that L should be close to or higher than the number of samples in one period of the lowest frequency component.

Step 1.2 – Singular value decomposition (SVD): Matrix Y is decomposed into the product of three matrices: an orthogonal matrix U, a diagonal matrix S and the transpose of an orthogonal matrix V:

$$Y = USV^T \ (\ S\ =\ [diag(\sigma_1, \sigma_2, ..., \sigma_p), 0]) \tag{2}$$

where S is an $L \times K$ diagonal matrix. σ_p are the nonnegative values in decreasing order of magnitude and $p = \min\{L, K\}$. The diagonal entries of S are called the singular values of X.

Step 1.3 – Regroup the signals: The singular values are grouped by calculating the energy differential spectrum D_i [57] with a certain threshold η_σ:

$$D_i = \frac{\sigma_i^2 - \sigma_{i+1}^2}{(\sigma_i - \sigma_{i+1})^2},\ i = 1, 2, \ldots, (p-1) \tag{3}$$

$$\eta_\sigma = D_1/300 \tag{4}$$

where σ_i is the singular value, $\sigma_{\max}$ and $\sigma_{\min}$ denote the maximum and minimum of the singular values, respectively. D_i is the sequence of energy differential spectra, and p is the number of singular values. Singular value components m with D_i higher than η_σ are marked as signal-related components. The remaining singular values (p-m) are grouped as noise.

Step 1.4 – Reconstruction: The grouped sub-signals are reconstructed from a 2D matrix to a time series using the anti-diagonal averaging method [58]:

$$y_{rc,k} = \begin{cases} \dfrac{1}{k} \displaystyle\sum_{m=1}^{k} y^*_{m,k-m+1} & 1 \leqslant k < L^* \\ \dfrac{1}{L^*} \displaystyle\sum_{m=1}^{L^*} y^*_{m,k-m+1} & L^* \leqslant k \leqslant K^* \\ \dfrac{1}{N-k+1} \displaystyle\sum_{m=k-K^*+1}^{N-K^*+1} y^*_{m,k-m+1} & K^* \leqslant k \leqslant K^* \end{cases} \tag{5}$$

where $L^* = \min(L, K)$, $K^* = \max(L, K)$, and when $L < K$, $y_{ij}^* = y_{ij}$ otherwise $y_{ij}^* = y_{ji}$, and $y_{ij}^* = y_{ij}$ is the element in Y. After SSA, the strong broadband noise signals are filtered efficiently.

Step 2: VMD.

VMD decomposes signal X into an ensemble of band-limited intrinsic mode functions (IMFs) $u_k(t)$ [47], where k is the number of modes.

Step 2.1 – The construction variational problems: After applying the Hilbert transform, frequency mixing, and the heterodyne demodulation, this problem is described as:

$$\begin{cases} \min\limits_{\{u_k\},\{\omega_k\}} \left\{ \displaystyle\sum_{k=1}^{K} \left\| \partial_t \left[\left(\delta(t) + \frac{j}{\pi t} \right) u_k(t) \right] e^{-j\omega_k t} \right\|_2^2 \right\} \\ \text{subject to} \quad \displaystyle\sum_{k=1}^{K} u_k = X \end{cases} \tag{6}$$

where $(\delta(t) + j/\pi t)\, u_k(t)$ is the unilateral frequency spectrum pf sub-signals u_k, and $\delta(t)$ is the Dirac distribution, $\{u_k\} = \{u_1, \ldots, u_k\}$ and $\{\omega_k\} = \{\omega_1, \ldots, \omega_k\}$ are shorthand notations for set of all modes and their center frequencies, respectively. ∂_t refers to the gradient with respect to t. $||\cdot||^2$ is the L_2 norm.

Step 2.2 – Solving the variational problem: The constrained variational problem is converted to an unconstrained variational problem by introducing augmented Lagrange [47]. The Alternate Direction Method of Multipliers (ADMM) is introduced to solve the unconstrained variational problem [59]. All the modes in the frequency domain $\widehat{U}_k^{n+1}$ and corresponding centre frequency ω_k^{n+1} are expressed as:

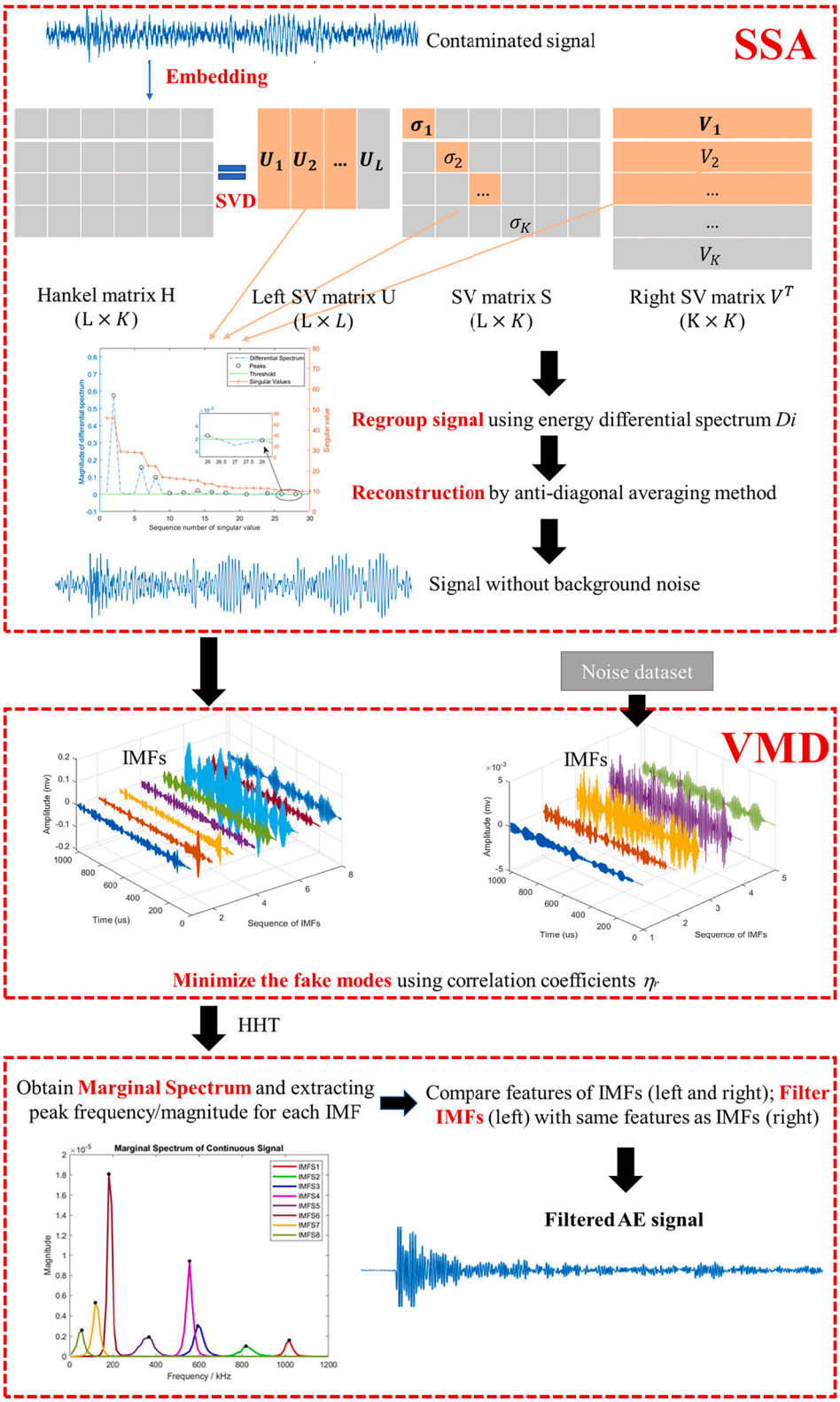

Fig.1. Framework of SSA-VMD.

$$\widehat{U}_k^{n+1}(\omega) = \frac{\widehat{f}(\omega) - \sum_{i \neq k} \widehat{U}_i(\omega) + \lambda(\omega)/2}{1 + 2\alpha(\omega - \omega_k)^2} \tag{7}$$

$$\omega_k^{n+1}(\omega) = \frac{\int_0^\infty \omega |\widehat{U}_k(\omega)|^2 d\omega}{\int_0^\infty |\widehat{U}_k(\omega)|^2 d\omega} \tag{8}$$

Eq. (7) represents the Fourier representation of a Wiener filter with power spectrum prior $1/(\omega - \omega_k)^2$ to ensure robust noise resilience for the algorithm. The Fourier transform of u is denoted as $\widehat{U}$. α is the quadratic penalty term and λ (w) is the Lagrangian multipliers. Sud [60] discussed the possibility to determine the number of modes K a priori. The results show K=6 to 10 is suitable for wideband interferers. Considering the AE signals are distributed in a wide-band frequency range, K=8 is selected in this case, which means 8 IMFs are obtained after this step.

Step 2.3 – Minimize the fake modes: The correlation coefficients between the decomposed IMFs and the original signal is calculated, and a threshold is then to be defined as:

$$\eta_r = \rho \cdot R_{\max} \tag{9}$$

where $R_{\max}$ is the calculated maximum correlation coefficient, ρ is the ratio between the threshold and $R_{\max}$, and ρ is equal to 0.025 in the following analysis after trials in certain cases. The modes with a correlation coefficient lower than η_r will be regarded as fake modes and removed. This step is significant because fake modes are common in real applications.

Step 2.4 – Use marginal spectrum to filter IMFs: Marginal spectrum (MS) based on the Hilbert-Huang spectrum (HHT) is an innovative approach for analyzing non-stationary and nonlinear signals [45]. The peak frequency and magnitude of the decomposed IMFs (via VMD) of the noise database can be identified using MS.

To improve the accuracy and avoid the error modes generated by spectral leakage, the density-magnitude index (DMI) is proposed to find the noise-related IMFs with the greatest possibility:

$$\mathrm{DMI}(f_i) = \mathrm{num}(f_i)/N_{\mathrm{noise}} + \rho_M \times \mathrm{normalization}(\overline{M(f_i)}) \tag{10}$$

where DMI(f_i) is the value of DMI under peak frequency f_i; num (f_i) is the number of IMFs with peak frequency f_i in the noise dataset; N_{noise} is the total number of IMFs in the noise dataset; ρ_M is determined as 0.3 as the weight factor; $\overline{M(f_i)}$ is mean magnitude for IMFs with frequency f_i. The first term describes the density of IMFs in the noise dataset with a specific peak frequency f_i. The second term is the magnitude according to which the noise principal components are of dominant energy. The likelihood of noise-related IMFs increases with a higher density and magnitude. In this study, f_i with DMI larger than 0.03 is regarded as the main frequency feature of noise-related IMFs.

After recognizing the dominant frequency characteristics of the noise database, the IMFs of AE signals after step 2.3 with the same frequency features as that of noise database can be filtered. Then, the denoised AE signals can be reconstructed using the remaining

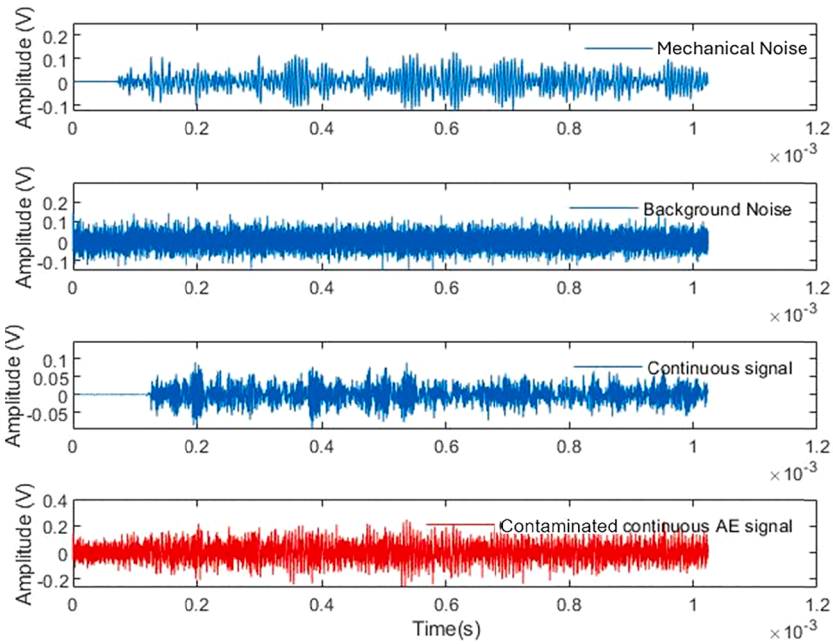

Fig.2. Illustration of a contaminated continuous signal with SNR=-5 dB.

IMFs.

3. Evaluation of SSA-VMD method

3.1. Framework of SSA-VMD for denoising

A framework of SSA-VMD to denoise the AE signals is shown in Fig. 1. First, a numerical simulation is performed to test the performance of the denoising method. Two types of noise exist in the laboratory environment of steel tensile deformation tests: wideband background noise, and narrowband mechanical noise (including friction noise and engine noise). Consequently, as shown in Fig. 2, background noise (X_B) and mechanical noise (X_M) are mixed with the original AE signal ($X_{AE,C}$) to obtain a contaminated signal (X_C).

AE signals can be generally classified into two basic types: (1) A burst AE signal with a clear pick and the following ringdown. (2) A continuous AE signal which is a convolution of small burst signals. Continuous signals are more likely to be obscured by noise than burst-shape AE signals. Besides, continuous signals are compatible with the dislocation movement or plastic deformation of material generated during steel deformation [35,61]. Hence, in this simulation, a continuous signal is selected as the original signal. The original AE signal $X_{AE,C}$ is a continuous signal from the pencil lead break test on a steel specimen. X_B is white noise simulated by Matlab with wideband frequency and X_M is a detected AE signal at the beginning of a steel tensile test under a low load level. This signal can be regarded as the detected mechanical noise without any damage or dislocation movement in the material. The AE acquisition system and sensor used to record $X_{AE,C}$ and X_M are identical. Fig. 3 shows the frequency spectrum of the original AE signal and noise. Signal to noise ratio (SNR) is introduced to quantify the influence of the noise as:

$$SNR = 10 \times \log_{10}\left(\sum_{i=1}^{N} x(i)^2 / \sum_{i=1}^{N} y(i)^2\right) \tag{11}$$

where $x(i)$ is the original signal and $y(i)$ is the noise signal; N is the length of the signal. The SNR of the contaminated signal in this simulation is calculated as -5 dB. The negative SNR represents practical cases with strong noise conditions (SNR$<$0), which means that the original signal is submerged into the noise signals.

3.2. Denoising results by SSA-VMD

Fig. 4 shows the overview of the denoising process for the contaminated continuous AE signal (X_C). The anticipated results after each step are correspondingly illustrated on the right side of the dashed line. In this simulation, X_M is the noise dataset to provide the features of narrow-band noise. The number of rows L of the Hankel matrix in step 1.1 is determined as follows. AE signals are measured by the AE acquisition system in the operating frequency range of 100 kHz $-$ 1000 kHz. The sampling frequency F_s is 10 MHz with a time resolution Δ_t of 1×10^{-7} s. The corresponding maximum number of samples in the period is calculated as:

$$n_{max} = T_{max}/\Delta_t = (1/100\ \text{kHz})/(1 \times 10^{-7}) = 100 \tag{12}$$

Hence, SSA can obtain good performance with L>100. To achieve a trade-off between the accuracy and calculation speed, L is defined as $N/64 = 160$, where N is the total number of samples in one signal. The comparison of $X_{AE,C}$ vs X_C^2 and X_M vs X_M^2 in the time domain and frequency domain is shown in Fig. 5. It implies that the original signal $X_{AE,C}$ and mechanical noise can be regrouped effectively.

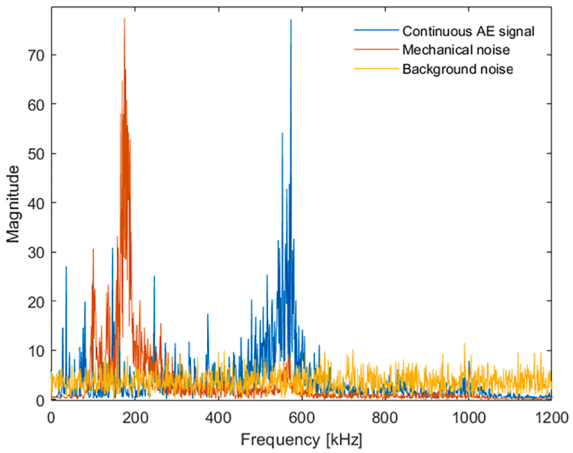

Fig.3. Frequency spectrum of AE signals and noise signals.

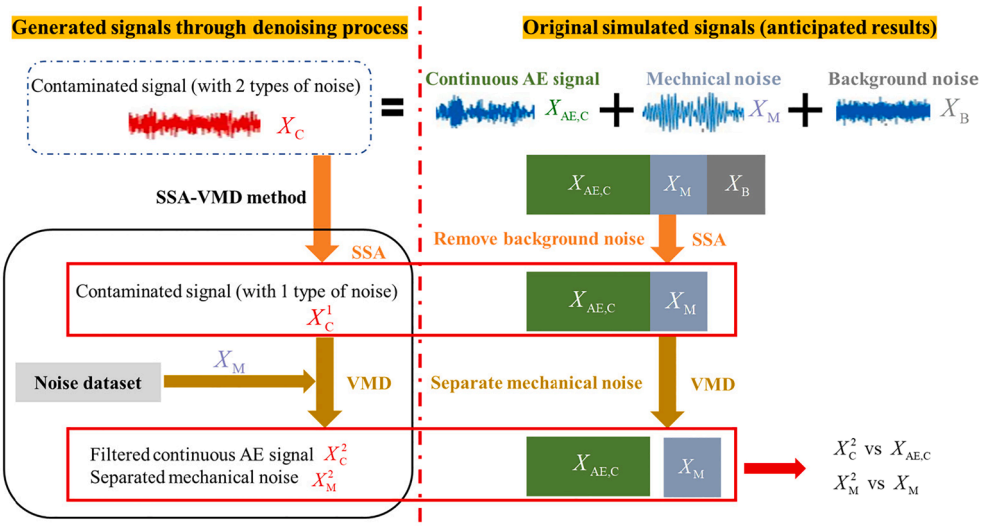

Fig.4. Overview of the evaluation of the SSA-VMD method.

3.3. Comparison with other methods

Various signal-denoising methods are introduced for comparison, including WT, SSA, and VMD, SSA-VMD proposed by Xiang [54], and our proposed SSA-VMD method. The configurations of these comparison methods are detailed in Table 1. For WT denoising, the decomposition level L_{WT} is selected as 5 to achieve high-frequency resolution, considering the sampling frequency. It is recommended to use high-order wavelet functions to mitigate energy leakage issues [62]. Therefore, a high-order Mother wavelet 'sym30' is employed as the wavelet function for analysis. SSA is not suitable for denoising the narrow-band mechanical noise. The optimal number of Hankel matrix rows L is determined with numerical analysis to improve the denoising quality. L is equal to 500 after checking the distribution of the DR index [55] with the various number of rows. For the VMD method, the resulting IMFs are filtered according to the similarity of their peak frequencies with those of the IMFs obtained from a noise dataset.

Xiang's method involves two key steps: (1) using SSA to decompose the original time series data into various independent components, including the main signals and residual signal; (2) further decomposing the residual parts into several sub-layers using the adopted VMD technique. Notably, this hybrid method does not take the noise dataset into consideration. For comparative purposes, identical parameter settings are applied to both hybrid methods. To evaluate the denoising effectiveness, Root-mean-square (RMS) values between the filtered signals X_C^2 and the original signal $X_{AE,C}$ are calculated as the indicator:

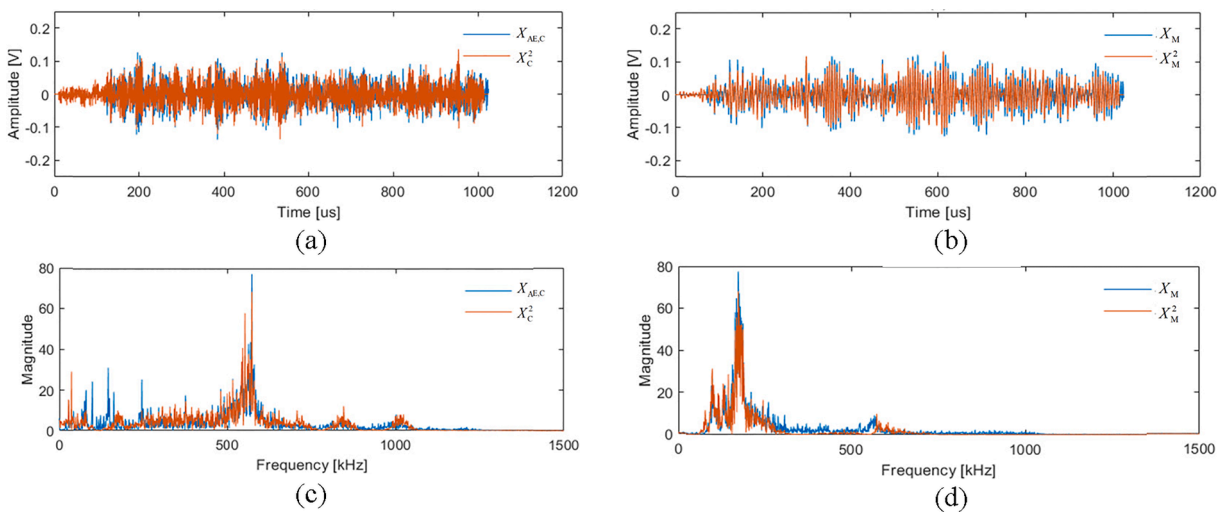

Fig.5. Comparison between: (a) and (b) $X_{AE,C}$ vs X_C^2, (c) and (d) X_M vs X_M^2

Table 1
Comparison of various denoising methods.

Method	Adaptivity	Options	Value	Calculation time (s)	RMS
WT	No	Mother wavelet	sym30	2.53	0.0362
		Decomposition level	5		
SSA	No	Hankel matrix size	500 × 500	102.3	0.0228
		Window length	160		
VMD	No	Decomposition modes	8	3.17	0.0246
Xiang et al. [54]	Yes	Hankel matrix size	500 × 500	6.74	0.0441
Proposed SSA-VMD	Yes	Window length	160	9.22	0.0191
		Decomposition modes	8		

$$RMS = \sqrt{\frac{1}{N}\sum_{i=1}^{N}\left[X_C^2(i) - \left(X_{AE,C}\right)\right]^2} \tag{13}$$

where N is the signal length. Table 1 shows the denoising results using three methods.

Fig. 6 shows the time–frequency plot of the original signal, noisy signal, and filtered signals using different methods. It is found that: (1) WT, SSA, and VMD are non-adaptive methods which need simulations to find appropriate setting parameters. (2) The proposed SSA-VMD outperforms other methods in terms of denoising accuracy with the lowest RMS; while the WT method failed to filter the noise around 200 kHz and part of the primary component was lost. (3) By incorporating information from the noise dataset, the VMD method effectively filtered out noise around 200 kHz. However, this process also resulted in a loss of signal power in the frequency of interest. With optimized parameter settings, it may be possible to avoid this loss of signal. (4) The hybrid method proposed by Xiang is

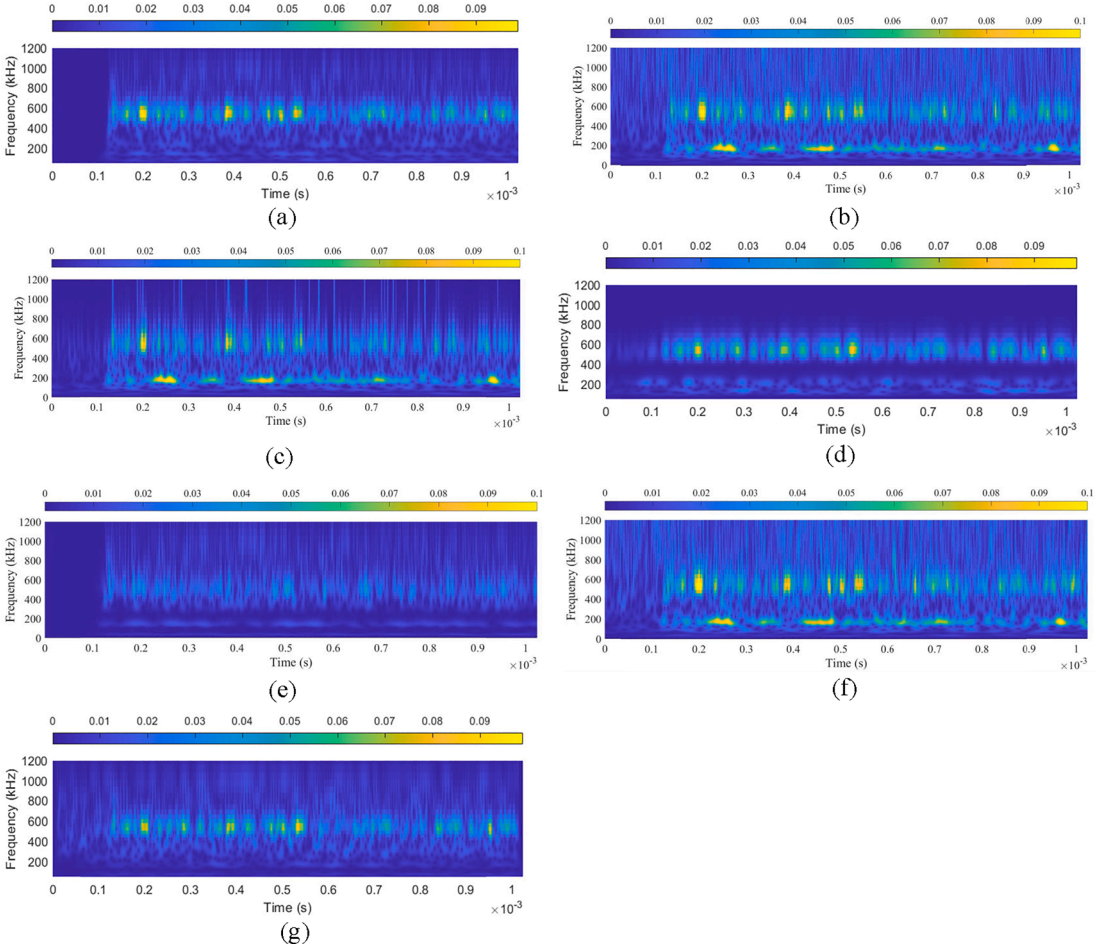

Fig.6. Time-frequency plot of (a) original signal $X_{AE,C}$, (b) noisy signal X_C, and filtered signals by (c) WT, (d) SSA, (e) VMD, (f) SSA-VMD proposed by Xiang [54], and (g) proposed SSA-VMD.

not able to effectively filter the noise, as its original design aims to reduce the instability of the data rather than for de-noising purposes. (5) As for the computation time, WT is the fastest method. However, the time for prior selection of wavelet function and decomposition level is not included. These above observations demonstrate that SSA-VMD can eliminate the background noise and mechanical noise effectively while generally preserving the characteristics of the original signal.

4. Experimental studies

4.1. Experimental set-up

The SSA-VMD method is applied for the AE measurement of steel tensile deformation. Tensile coupon tests were performed to collect the AE signals during tensile steel deformation. As shown in Table 2, ten coupons were cut from cold-formed square steel tubes with three steel grades (S355, S500, and S700) and an identical cross-section area (80 mm^2). Fig. 7 describes the profiles of the coupon specimens. The overview of the experimental set-up is shown in Fig. 8. Tensile tests were performed in an Instron testing machine with a maximum loading of 100 kN with displacement control. The deformation is measured by a 50 mm extensometer. The AE acquisition system used for the tensile tests consists of a physical AEwin system software with two piezoelectric sensors VS600-Z2 and pre-amplifiers with a uniform gain of 40 dB. The sensors were attached to the specimen symmetrically using a hot-melt adhesive. Before each test, pencil leads breaking tests were carried out to calibrate the response of the AE sensors. As shown in Fig. 8 (b), the frequency range of VS600-Z2 is 200 kHz-1000 kHz with a resonant frequency of around 600 kHz. It is reported that the predominant AE frequency range for metallic structures is 100 kHz-900 kHz [63]. Although the VS600-Z2 sensor is less sensitive in the range from 50 kHz to 200 kHz, it does also measure in this range. This sensor is chosen due to the limited space for the sensor. The operational frequency range of the AE acquisition system is set as 100 kHz – 1000 kHz. It has been demonstrated that the amplitude of AE signals from plastic deformation ranges from 30 to 60 dB [64]. The threshold was set to 30 dB to capture signals generated during deformation.

Considering constant loading is not applicable in many practical cases, varying loading rates were applied for the tensile tests (see Fig. 9). The selected loading rate meet the requirement of the Eurocode (0.01 m/s to 0.10 m/s). The loading rate of 0 mm/s means the holding stage and −0.01 mm/s represents the unloading stage. Fig. 9 shows the amplitude distribution of detected signals along the tensile process. It is found that numerous signals appeared at the beginning and unloading–reloading stages. The following factors contributes to this phenomenon: (1) The friction noise is generated due to the contact between the grip and specimen at the beginning and during the unloading–reloading stage; (2) the engine noise is from the vibration of the fluid pump in the loading frame. Hence, these signals can be classified in the noise database. The amplitude of these signals is up to 50 dB which can overlap the useful signals from plastic deformation. This produces a justification for applying an appropriate denoising method.

4.2. Experimental validation

The effectiveness of the utilized SSA-VMD in denoising the measured AE signals is illustrated in this section. Denoising of the recorded AE signals from specimen S700-1 is taken as an example. In the previous simulation evaluation, only one mechanical noise signal constitutes the noise database. The noise dataset during the tensile test consists of a large number of signals. The marginal spectrum of decomposed IMFs of detected AE signals in step 2.4 is calculated and shown in Fig. 10. The X-axis is the sequence of IMFs. The y-axis and Z-axis are the extracted peak frequency and magnitude of each IMF. It is observed that four specific frequency ranges (red dash boxes) exist along all deformation procedures. There is a possibility that the IMFs located in these frequency ranges could be related to noise. Then, 18 peak frequencies are extracted as the main frequency components of noise-related IMFs with DMI>0.03. The IMFs of the detected AE signals are filtered if they have the same frequency features as the extracted 18 peak frequencies from the noise dataset.

The amplitude distribution of the filtered signals of S355-1 and S700-1 is shown in Fig. 11. Compared to Fig. 9, AE signals recorded at the beginning and during loading–unloading stages under low load levels disappear. It is noted that the amplitude of remaining AE signals is decreased which is attributed to that part of the power of the initially detected AE signals is generated by noise.

Table 2
Properties of coupon specimens.

Sample	Geometry features		Unloading	Loading rate
	Nominal thickness t (mm)	Width b_0 (mm)		
S355-1	10	8	No	Varying
S355-2	10	8		Varying
S355-3	6	13.3		Varying
S355-4	6	13.3		Constant
S500-1	8	10	Yes	Constant
S500-2	10	8		Varying
S500-3	10	8		Constant
S700-1	10	8	Yes	Constant
S700-2	8	10		Varying
S700-3	8	10		Constant

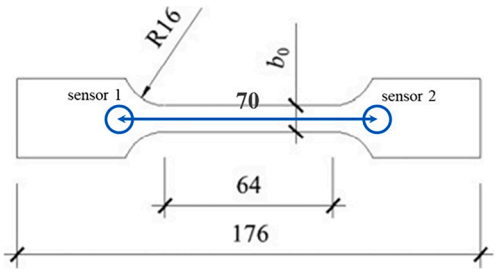

Fig.7. Profiles of the coupon tensile specimens in mm [6].

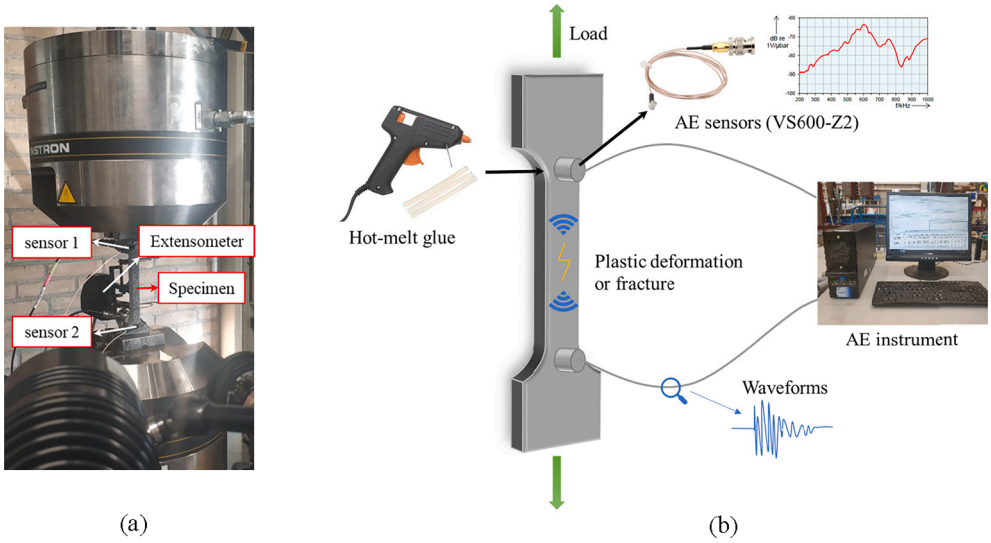

Fig.8. Diagram of (a) Experimental set-up and (b) AE schematic.

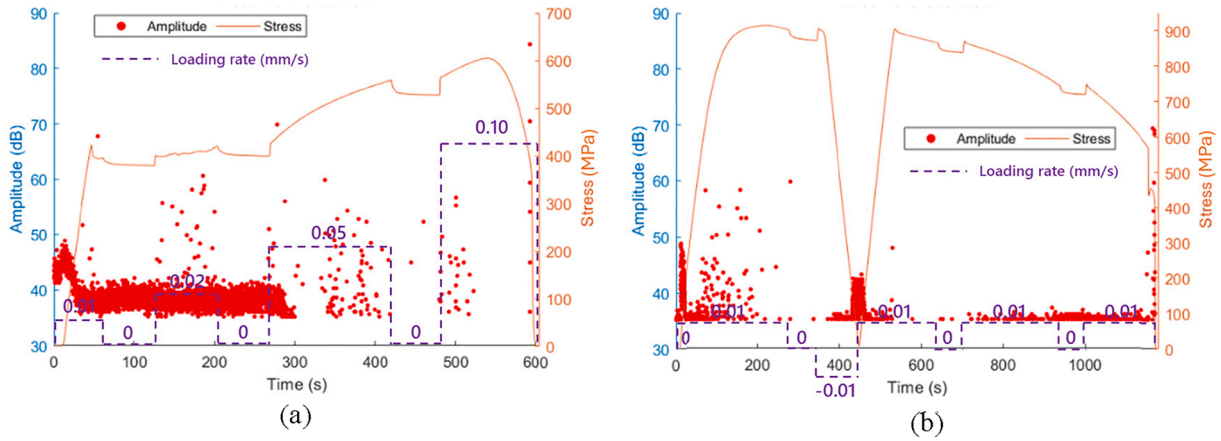

Fig.9. Amplitude distribution of detected signals for (a) S355-1 and (b)S700-1.

5. Application of ANN for classification

5.1. Introduction to the methodology

To identify the deformation stages of steel material, ANN is employed to establish the relationship between AE parameters and deformation stages. The algorithm of a fully connected neural network (FCNN), one typical type of ANN, is commonly used in material

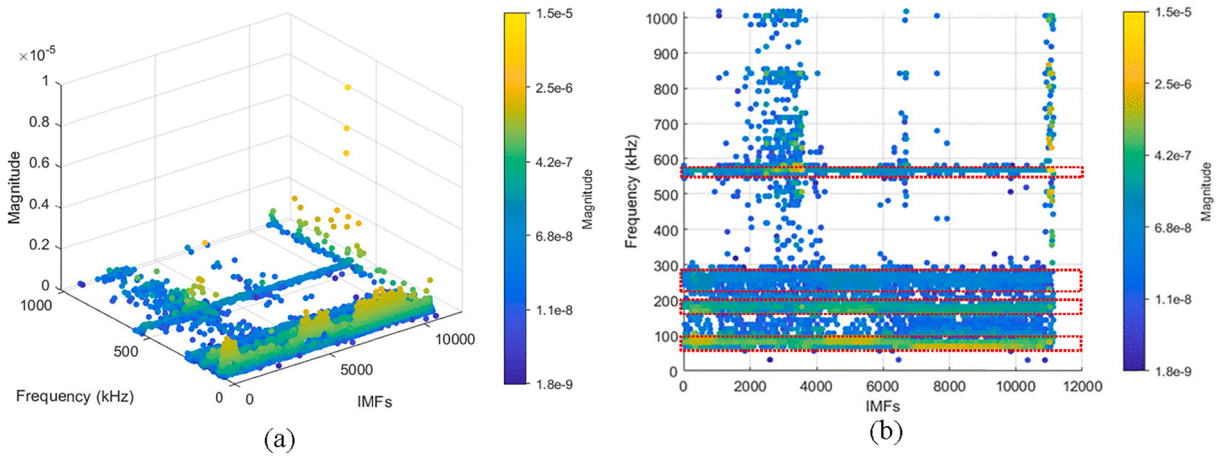

Fig.10. Features of decomposed IMFs of detected AE signals of S700-1: (a) 3D plot and (b) top view.

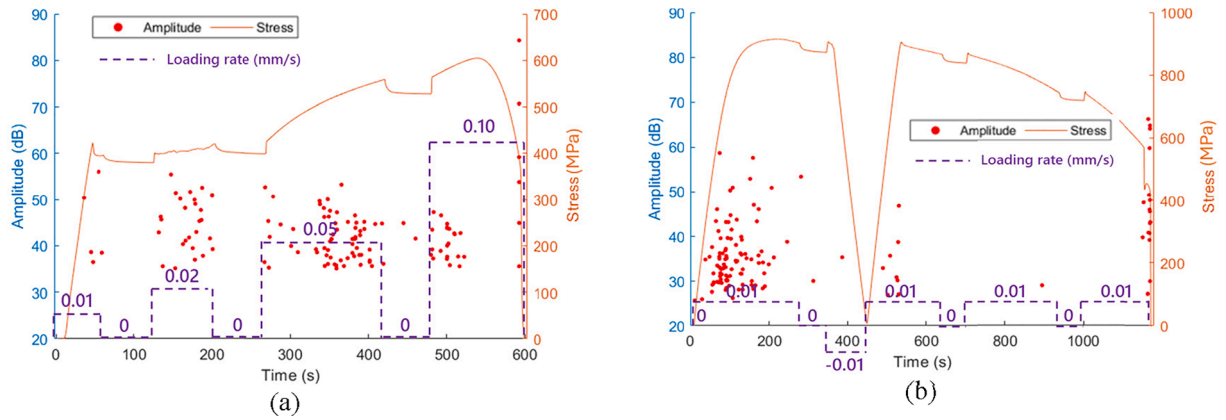

Fig.11. Amplitude distribution of filtered signals for (a) S355-1, and (b) S700-1.

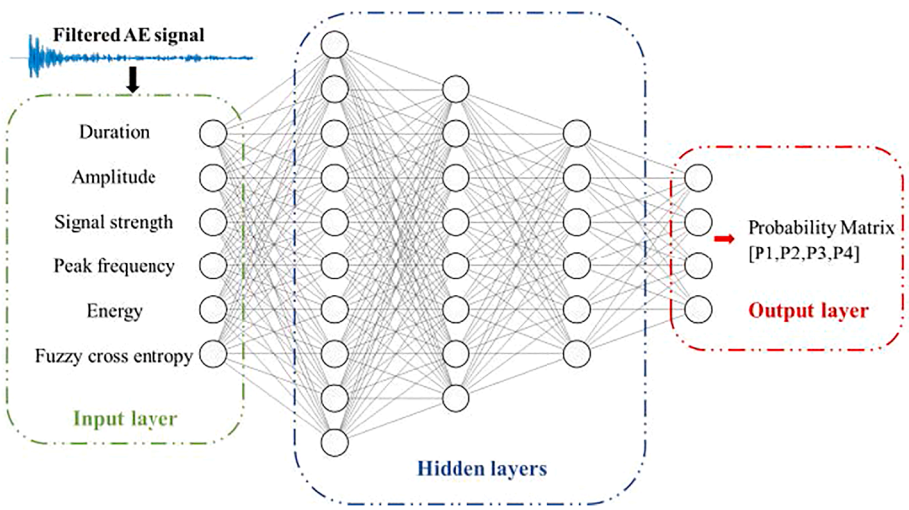

Fig.12. Schematic of the applied ANN.

and structural damage identification [13]. Typically, a FCNN consists of an input layer, hidden layers, and an output layer, as shown in Fig. 12. Neurons in hidden layers combine values from the input layers transformed by communication links. A similar denoising procedure as described in section 4.2 is applied to all specimens. After that, the AE parameters, including amplitude, duration, signal strength, peak frequency, energy, and fuzzy cross-entropy, are extracted from the filtered AE signals as the input. Except for these conventional AE features, fuzzy cross-entropy has been proposed to interpret time-series signals recently [65,66]. This feature is useful to describe the complexity of AE signals with high sensitivity.

Generally, according to the appearance of a distinct plateau, steel materials can be classified as discontinuous yielding and continuous yielding materials (see Fig. 13). Various deformation stages are included in these two materials. It is well recognized that the AE signals depend on the AE source mechanisms. Before the 1970 s, it was traditionally believed that AE signals could not be recorded prior to macro-yielding, as there was no dislocation activity or elastic wave release [67]. However, subsequent studies [68–70] have demonstrated that AE signals can be generated due to partial dislocation multiplication and harmonic motion before the material reaching its elastic limit. During the yielding and strengthening stage, the AE source mechanism is the dislocation multiplication inside the material. When the specimen enters the necking stage, the specimen exhibited significant deformation. The freedom for further dislocation shrank significantly with considerable dislocation congestion. Meanwhile, the formation of microcracks also reduces the transmission of AE activity. Finally, the abrupt decrease in stress is followed by a sudden increase in the AE activity and amplitude of AE signals. The specimen starts to develop microscopic cracks and keeps growing until the final fracture. Hence, stage AB and BC in discontinuous yielding material is summed into one stage. In total, no matter for discontinuous or continuous yielding material, four deformations stages are identified. Correspondingly, the output layer is a 4×1 vector [P1, P2, P3, P4] to represent the different deformation stages (see Fig. 13): [1, 0, 0, 0] represents the elastic stage; [0, 1, 0, 0] represents the strengthening stage; [0, 0, 1, 0] represents the necking stage; [0, 0, 0, 1] represents the final fracture stage. For S500 and S700 steel, an offset yield of 0.2 % ($R_{p0.2}$) is used to determine the yield point A for these materials [71].

5.2. Architecture of the network

Table 3 summarizes the number of collected signals during the tensile tests. The samples are in unbalanced distribution for different stages which will decrease the prediction accuracy or generalization of the network. Focal loss is selected as the loss function to address the class imbalance problem. A modulating factor $(1\text{-}p_t)^{\gamma}$ and a weight factor α_t can adjust the weight of samples from each class for the multi-classification problem. The focal loss is designed as:

$$FL(p_t) = -\alpha_t(1-p_t)^{\gamma}\log(p_t) \tag{14}$$

In practice, optimal values for α_t and γ are determined through empirical studies [72]. In this study, weight factors α_t are set as 1.5, 0.25, 2, and 1 for identifying elastic, strengthening, necking, and fracture stages, respectively. Higher weight factors are used in the elastic and necking stages due to their smaller datasets. Despite fewer AE signals collected during the fracture stage, a smaller weight factor is applied. This is attributed to the distinct features of the fracture stage, making it easily distinguishable from the other three stages.

The K-fold cross-validation technique is utilized to train the network for classification with robustness to the overfitting problem. This method is one of the most widespread validation techniques in machine learning [73–77]. In this method, the training data are randomly partitioned into K folds. For each fold, a classifier is trained on the remaining folds. The average of these K recorded accuracy serves as the performance measure. This approach is particularly beneficial when the sample dataset is limited due to experimental constraints or the impossibility of repeating the experiment to obtain more training data. Hence, all examples are used at least once for both training and testing [78].

A cross-validation with K=5 was applied in this study. As illustrated in Fig. 14, the data set is randomly split into a test set (20 %) and a training set (80 %) with a training fold (64 %) and 5 disjoint validation folds (16 %). Hyperparameter tuning is conducted to find the optimal solution. Hyperparameters include the learning rate η and the number of hidden layers is fine-tuned using grid search. Quantitative evaluation is provided by 5 indexes: Accuracy (ACC) and four areas under receiver operating characteristics (ROC) curves (AUC_i, $i = 1{:}4$). Accuracy (ACC) is defined as the correct number of predictions divided by the number of total data. This represents the total effectiveness of the classification. AUC_i measures the performance for each deformation stage classification. The average of these 5 indexes is employed as the indicator for the prediction accuracy. Based on the results of hyperparameters tuning, the optimal architecture is illustrated in Fig. 12 and the main hypeparameters are summarized in Table 4. In the input layer, 6 input neurons represent duration, amplitude, signal strength, peak frequency, energy and fuzzy cross-entropy respectively. 3 hidden layers are set with 12, 8 and 6 artificial neuron units, respectively. The neuron units have 2 functions: a linear combination of input with regulated weightage and nonlinear complex functional mapping by ReLU activation functions. The output layer contains 4 neuron units which represent the possibility of 4 different deformation stages. The activation function is Softmax, which is appropriate for the multi-classification problem.

5.3. Training results and discussion

To increase the converging speed, the training set is normalized before it is input into the networks. Fig. 15 illustrates the training history of loss and learning curves for the training and test dataset. The loss and accuracy values are shown in every 1 epoch and the maximum number of epochs employed in this study is 200. The loss begins with 0.45 and then a dramatic decrease tendency is

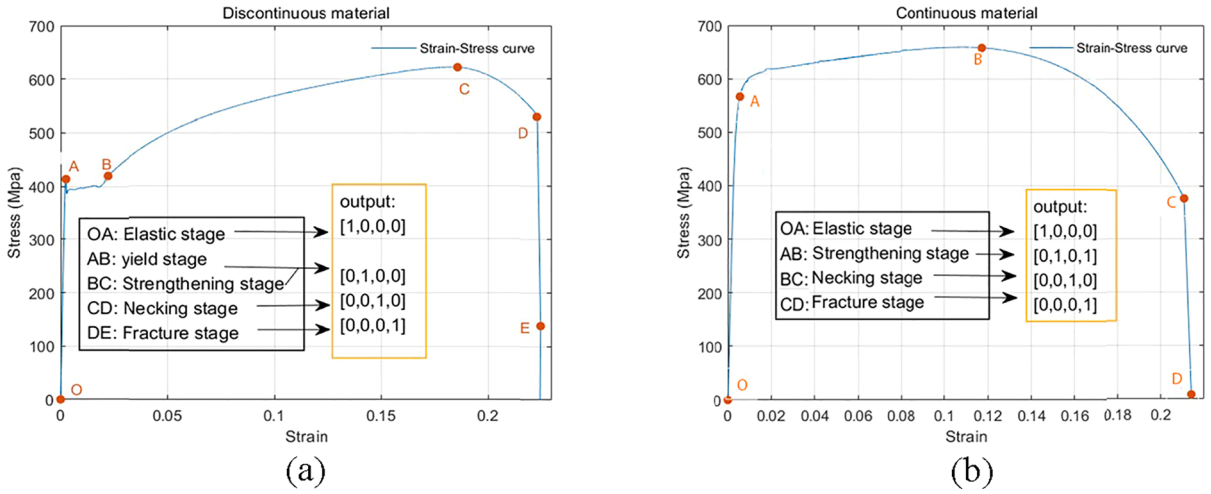

Fig.13. Strain-stress curve for steel material: (a) discontinuous yielding material, and (b) continuous material.

Table 3
Collected signals for machine learning-based analysis.

Name	Number of data				
	Elastic stage	Strengthening stage	Necking stage	Fracture stage	Total
S355-1	7	12	4	4	27
S355-2	2	155	1	101	259
S355-3	13	532	1	11	557
S355-4	15	386	1	52	454
S500-1	1	5	7	3	16
S500-2	18	5	3	7	33
S5003	35	41	43	7	126
S700-1	173	62	42	147	424
S700-2	75	1112	0	99	1286
S700-3	96	88	10	27	221
Total	435	2398	112	458	3403

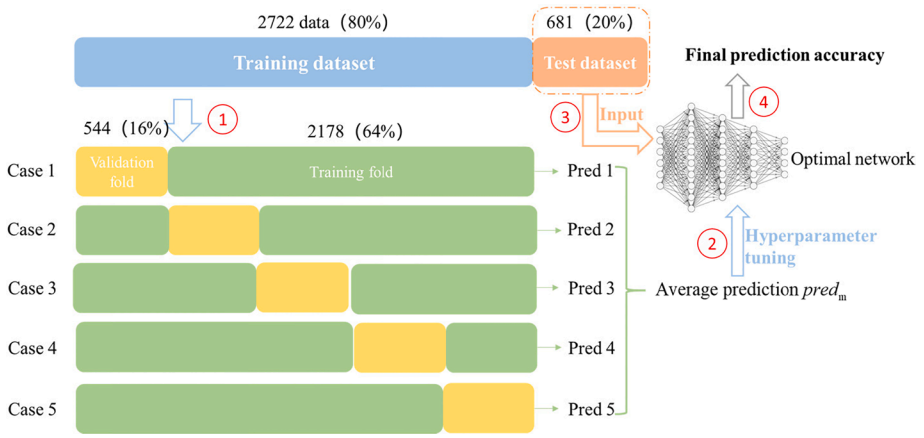

Fig.14. Process of k-fold cross validation.

Table 4
The main hyperparameters of the proposed ANN.

Learning rate	Number of hidden layers	Epoch	Batch size	Optimizer	Loss function
0.04	3	200	1000	Nadam	focal loss

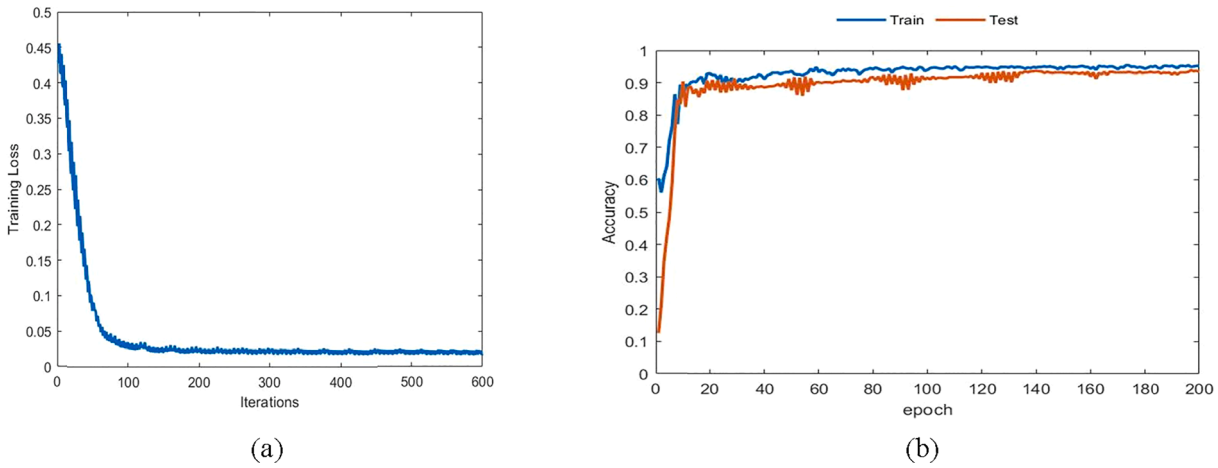

Fig.15. (a) Loss and (b) learning curves of the optimized FCNN.

observed until 100 iterations. Then the curve is flat indicating convergence. As indicated in Fig. 15 (b), the training curve starts with an accuracy of 0.6 which can be contributed to the good initial parameter setting. From 1 to 20 epochs, the accuracy rises rapidly and reaches 0.9 after 20 epochs for training and test dataset. Finally, the accuracy curve converges to an expected value of 0.93. The visualization of part classification results is shown in Fig. 16 and the corresponding accuracy index is summarized in Table 5. By

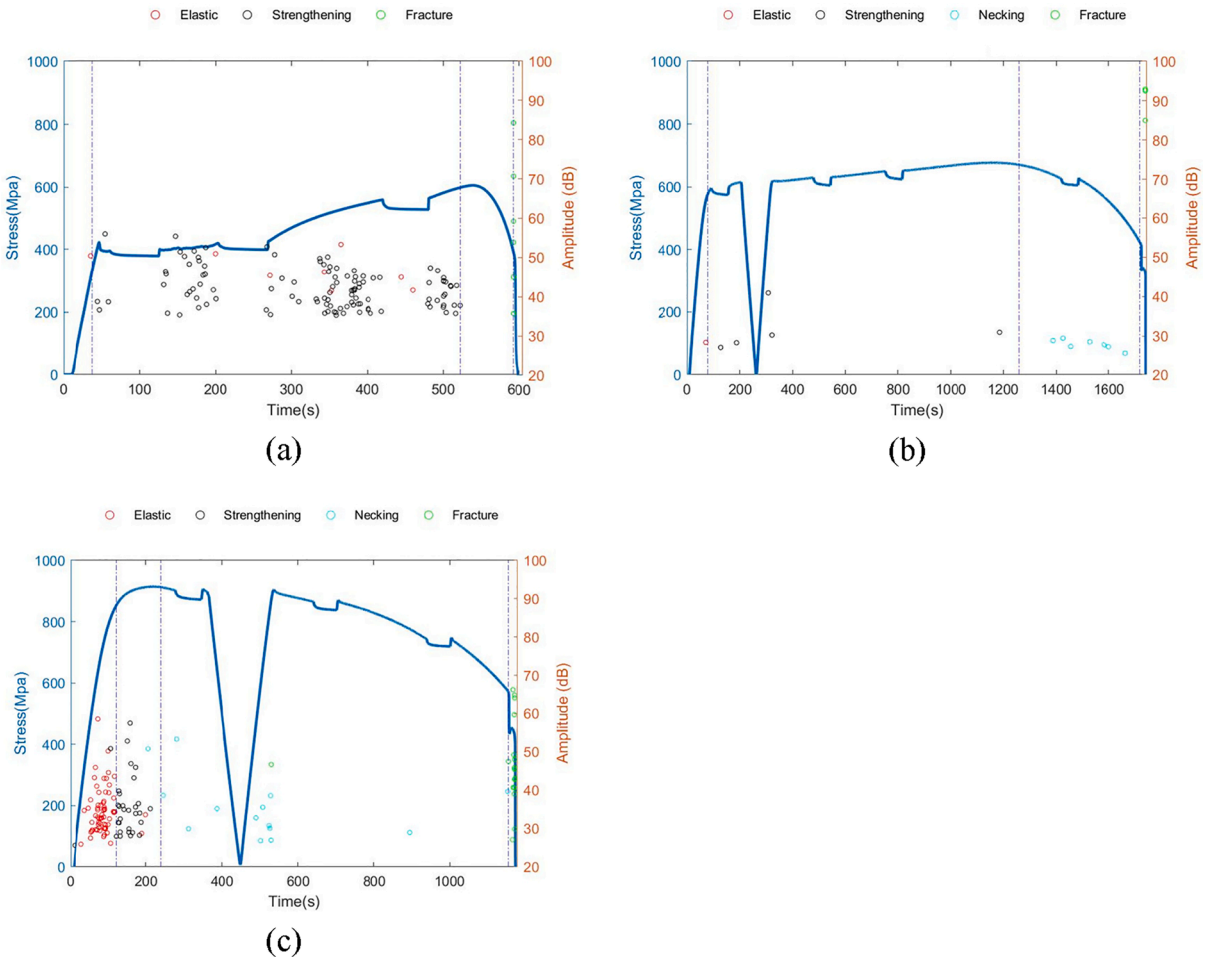

Fig.16. Classification results visualization (a) S355-1, (b) S500-1, and (c) S700-1.

Table 5
Classification accuracy for each specimen.

Material	Name	Accuracy
Discontinuous material	S355-1	0.963
	S355-2	0.950
	S355-3	0.922
	S355-4	0.958
Continuous material	S500-1	1.000
	S500-2	0.848
	S500-3	0.941
	S700-1	0.939
	S700-2	0.906
	S700-3	0.824

omitting the unloading–reloading phase, discontinuous material specimens yield superior data quality, resulting in higher accuracy compared to continuous materials.

Network generalization describes how well a trained network performs with new data [79]. Unseen data is collected from a continuous material specimen S700-4, with 8 mm thickness and constant loading rate. The specimen was tested under the same test setup and AE acquisition system. The collected AE signals are denoised by SSA-VMD with identical parameters as previously described. Fig. 17 shows the classification results for S700-4. The prediction accuracy is 0.87 which is smaller than 0.93 for the test dataset. Despite the decrease in accuracy, the results still demonstrate the efficiency of the trained ANN. It demonstrates the potential of applying ANN-based deformation stage identification for various steel materials.

6. Conclusion

The deformation of the steel member is vitally important to the safety of infrastructure. Identification of the deformation stage is possible to be achieved using an Artificial neural network (ANN) combined with Acoustic emission (AE) monitoring. However, the efficiency is hindered by the existence of noise in practical applications. The main objective of this study is to improve the application of ANN-based deformation stage identification with a hybrid denoising model combing SSA-VMD method. The key finding can be concluded as follows:

1. The two-stage decomposition method SSA-VMD is an adaptive algorithm for filtering both wide-band ground noise and narrow-band mechanical noise effectively. This method provides the solution to select the proper parameters without the time-consuming numerical simulation.
2. Compared to conventional methods, the proposed SSA-VMD method can reduce noise while keeping relevant elements of the original signals under strong noise conditions (SNR$<$0). The denoising performance of the employed method has been validated and demonstrated by using the simulation signals and real signals during tensile tests.
3. The combination of SSA-VMD with ANN achieves the deformation stage identification successfully under a seriously noisy environment. Taking the features of filtered AE signals as the input, the designed ANN achieves a prediction accuracy of 0.93 for the test dataset and 0.87 for the unseen dataset. AE signals were collected from steel coupon tensile tests with various steel grades and loading conditions. The outcomes show the potential of ANN-based deformation stage identification in a broader application.

It should be noted that the collected AE signals are dependent on the applied sensors. The receiving and transmission sensitivity of

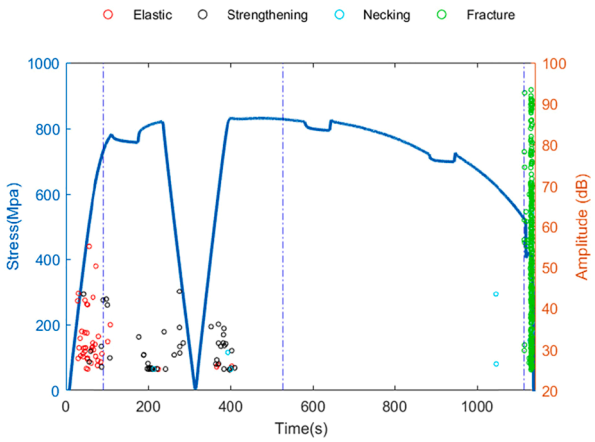

Fig.17. Classification results of S700-4.

the sensor will influence the extracted features. Although the effectiveness of the SSA-VMD method has been confirmed by the denoising results of simulation and measured signals, its universality demands investigating further with more experimental results. Meanwhile, it is suggested to provide support information from the microstructural examination to access the performance of the ANN-based deformation stage identification.

CRediT authorship contribution statement

Lu Cheng: Writing – review & editing, Supervision, Methodology, Data curation, Conceptualization. **Qingkun Sun:** Writing – original draft, Validation, Methodology, Investigation. **Rui Yan:** Writing – review & editing, Resources, Investigation. **Roger M. Groves:** Writing – review & editing, Supervision, Methodology. **Milan Veljkovic:** Writing – review & editing, Supervision, Resources, Methodology.

Declaration of competing interest

The authors declare that they have no known competing financial interests or personal relationships that could have appeared to influence the work reported in this paper.

Data availability

Data will be made available on request.

Acknowledgments

The first author wishes to express her gratitude for the financial support of the CSC Scholarship Council under grant number 201806060122.

References

[1] F. Sun, B. Xiao, Y. Zhang, Quantitative damage evaluation of LY225 steel under monotonic tensile loading based on acoustic emission entropy, J. Constr. Steel Res. 185 (2021) 106860, https://doi.org/10.1016/j.jcsr.2021.106860.
[2] A.M.P. De Jesus, R. Matos, B.F.C. Fontoura, C. Rebelo, L. Simões Da Silva, M. Veljkovic, A comparison of the fatigue behavior between S355 and S690 steel grades, J. Constr. Steel Res. 79 (2012) 140–150, https://doi.org/10.1016/j.jcsr.2012.07.021.
[3] F. Yang, M. Veljkovic, Y. Liu, Ductile damage model calibration for high-strength structural steels, Constr. Build. Mater. 263 (2020) 120632, https://doi.org/10.1016/j.conbuildmat.2020.120632.
[4] L.J. Jia, H. Kuwamura, Ductile fracture simulation of structural steels under monotonic tension, J. Struct. Eng. (United States). 140 (2014), https://doi.org/10.1061/(ASCE)ST.1943-541X.0000944.
[5] H.C. Ho, K.F. Chung, X. Liu, M. Xiao, D.A. Nethercot, Modelling tensile tests on high strength S690 steel materials undergoing large deformations, Eng. Struct. 192 (2019) 305–322, https://doi.org/10.1016/j.engstruct.2019.04.057.
[6] R. Yan, H. Xin, F. Yang, H. El Bamby, M. Veljkovic, K. Mela, A method for determining the constitutive model of the heat-affected zone using digital image correlation, Constr. Build. Mater. 342 (2022) 127981, https://doi.org/10.1016/j.conbuildmat.2022.127981.
[7] R. Yan, H. Xin, K. Mela, H. El Bamby, M. Veljkovic, Fracture simulation of welded RHS X-joints using GTN damage model, Adv. Struct. Eng. 2022 (2022) 1–20, https://doi.org/10.1177/13694332221137175.
[8] Y. Li, F. Xu, Structural damage monitoring for metallic panels based on acoustic emission and adaptive improvement variational mode decomposition–wavelet packet transform, Struct. Heal. Monit. 21 (2022) 710–730, https://doi.org/10.1177/14759217211008969.
[9] K. Schabowicz, Non-destructive testing of materials in civil engineering, Materials (Basel). 12 (2019) 3237, https://doi.org/10.3390/ma12193237.
[10] H. Xin, L. Cheng, R. Diender, M. Veljkovic, Fracture acoustic emission signals identification of stay cables in bridge engineering application using deep transfer learning and wavelet analysis, Adv. Bridg. Eng. 1 (2020) 1–16, https://doi.org/10.1186/s43251-020-00006-7.
[11] K.M. Holford, A.W. Davies, R. Pullin, D.C. Carter, Damage location in steel bridges by acoustic emission, J. Intell. Mater. Syst. Struct. 12 (2001) 567–576, https://doi.org/10.1106/KDNY-AJ0U-KP2B-P52R.
[12] A. Nair, C.S. Cai, Acoustic emission monitoring of bridges: review and case studies, Eng. Struct. 32 (2010) 1704–1714, https://doi.org/10.1016/j.engstruct.2010.02.020.
[13] L. Cheng, H. Xin, R.M. Groves, M. Veljkovic, Acoustic emission source location using Lamb wave propagation simulation and artificial neural network for I-shaped steel girder, Constr. Build. Mater. 273 (2021) 121706, https://doi.org/10.1016/j.conbuildmat.2020.121706.
[14] C.U. Grosse, M. Ohtsu, Acoustic emission testing, Springer Science & Business Media (2008), https://doi.org/10.1016/B978-0-12-804176-5.00028-1.
[15] H.L. Dunegan, D.O. Harris, C.A. Tatro, Fracture analysis by use of acoustic emission, Eng. Fract. Mech. 1 (1968) 105–122, https://doi.org/10.1016/0013-7944(68)90018-0.
[16] H.N.G. Wadley, C.B. Scruby, Cooling rate effects on acoustic emission-microstructure relationships in ferritic steels, J. Mater. Sci. 1991 2621. 26 (1991) 5777–5792. https://doi.org/10.1007/BF01130115.
[17] H.N.G. Wadley, C.B. Scruby, Spheroidal inclusion effects on acoustic emission-microstructural relations in ferritic steels, J. Mater. Sci. 1993 289. 28 (1993) 2517–2530. https://doi.org/10.1007/BF01151687.
[18] C.B. Scruby, H.N.G. Wadley, Tempering effects on acoustic emission-microstructural relationships in ferritic steels, J. Mater. Sci. 1993 289. 28 (1993) 2501–2516. https://doi.org/10.1007/BF01151686.
[19] C.K. Mukhopadhyay, K.K. Ray, T. Jayakumar, B. Raj, Acoustic emission from tensile deformation of unnotched and notched specimens of AISI type 304 stainless steels, Mater. Sci. Eng. A. 255 (1998) 98–106, https://doi.org/10.1016/s0921-5093(98)00771-0.
[20] S. Hao, S. Ramalingam, B.E. Klamecki, Acoustic emission monitoring of sheet metal forming: characterization of the transducer, the work material and the process, J. Mater. Process. Technol. 101 (2000) 124–136, https://doi.org/10.1016/S0924-0136(00)00441-6.
[21] J. Ahmed, T. Zhang, D. Ozevin, M. Daly, A multiscale indentation-based technique to correlate acoustic emission with deformation mechanisms in complex alloys, Mater. Charact. 182 (2021) 111575, https://doi.org/10.1016/J.MATCHAR.2021.111575.
[22] W. Zhou, Y.G. Du, S.D. Wang, Y.P. Liu, L.H. Ma, J. Liu, Effects of welding defects on the damage evolution of Q245R steel using acoustic emission and infrared thermography, Nondestruct. Test. Eval. (2022), https://doi.org/10.1080/10589759.2022.2094377.

[23] J. Yang, C. Zhang, H. Li, Y. Xia, Z. Yang, B. Pang, H. Wang, G. Sun, The development of deformation mechanism during tension at different strain rates for GH4169 superalloys quantified by in-situ acoustic emission, Mater. Today Commun. 33 (2022) 104239, https://doi.org/10.1016/J.MTCOMM.2022.104239.
[24] K. Barat, H.N. Bar, D. Mandal, H. Roy, S. Sivaprasad, S. Tarafder, Low temperature tensile deformation and acoustic emission signal characteristics of AISI 304LN stainless steel, Mater. Sci. Eng. A. 597 (2014) 37–45, https://doi.org/10.1016/j.msea.2013.12.067.
[25] C. Sun, W. Zhang, Y. Ai, H. Que, Study of the tensile damage of high-strength aluminum alloy by acoustic emission, Metals (Basel). 5 (2015) 2186–2199, https://doi.org/10.3390/met5042186.
[26] T. Haneef, B. Baran Lahiri, S. Bagavathiappan, C. Kumar Mukhopadhyay, J. Philip, B. Purna Chandra Rao, T. Jayakumar, Study of the tensile behavior of AISI type 316 stainless steel using acoustic emission and infrared thermography techniques, Integr. Med. Res. 4 (2015) 241–253, https://doi.org/10.1016/j.jmrt.2014.12.008.
[27] H. Sayar, M. Azadi, M. Alizadeh, Detection of crack initiation and propagation in aluminum alloy under tensile loading, comparing signals acquired by acoustic emission and vibration sensors, J. Nondestruct. Eval. 38 (2019) 100, https://doi.org/10.1007/s10921-019-0639-9.
[28] I. Lyasota, B. Kozub, J. Gawlik, Identification of the tensile damage of degraded carbon steel and ferritic alloy-steel by acoustic emission with in situ microscopic investigations, Arch. Civ. Mech. Eng. 19 (2019) 274–285, https://doi.org/10.1016/j.acme.2018.09.011.
[29] J. Xu, T. Sun, Y. Xu, Q. Han, Fracture toughness research of G20Mn5QT cast steel based on the acoustic emission technique, Constr. Build. Mater. 230 (2020) 116904, https://doi.org/10.1016/j.conbuildmat.2019.116904.
[30] A. Marchenkov, D. Chernov, D. Zhgut, A. Pankina, E. Rudenko, A. Poroykov, E. Kulikova, T. Kovaleva, Investigation of the scale factor impact on the results of acoustic emission monitoring of the steel specimens tension process, Appl. Sci. 12 (2022) 8280, https://doi.org/10.3390/APP12168280.
[31] J. Huang, Z. Zhang, C. Han, G. Yang, Identification of deformation stage and crack initiation in TC11 alloys using acoustic emission, Appl. Sci. 10 (2020) 3674, https://doi.org/10.3390/app10113674.
[32] S. Zou, F. Yan, G. Yang, W. Sun, The identification of the deformation stage of a metal specimen based on acoustic emission data analysis, Sensors (Switzerland). 17 (2017), https://doi.org/10.3390/s17040789.
[33] J. Vetrone, J.E. Obregon, E.J. Indacochea, D. Ozevin, The characterization of deformation stage of metals using acoustic emission combined with nonlinear ultrasonics, Measurement. 178 (2021) 109407, https://doi.org/10.1016/j.measurement.2021.109407.
[34] L. Zhang, S. Oskoe, H. Li, D. Ozevin, Combined damage index to detect plastic deformation in metals using acoustic emission and nonlinear ultrasonics, Materials (Basel). 11 (2018) 2151, https://doi.org/10.3390/ma11112151.
[35] L. Cheng, H. Xin, R.M. Groves, M. Veljkovic, Plasticity and damage characteristic of acoustic emission signals for S460 steel exposed to tensile load, in: Virtual Conf. Mech. Fatigue, University of Porto, Portugal, 2020. https://www.researchgate.net/publication/344235805_Plasticity_and_damage_characteristic_of_acoustic_emission_signals_for_S460_steel_exposed_to_tensile_load.
[36] A. Ebrahimkhanlou, J. Choi, T.D. Hrynyk, S. Salamone, O. Bayrak, Acoustic emission monitoring of containment structures during post-tensioning, Eng. Struct. 209 (2020) 109930, https://doi.org/10.1016/j.engstruct.2019.109930.
[37] J. Krajewska-Śpiewak, I. Lasota, B. Kozub, Application of classification neural networks for identification of damage stages of degraded low alloy steel based on acoustic emission data analysis, Arch. Civ. Mech. Eng. 20 (2020) 1–10, https://doi.org/10.1007/S43452-020-00112-3/TABLES/4.
[38] A. Stoll, P. Benner, Machine learning for material characterization with an application for predicting mechanical properties, GAMM Mitteilungen. 44 (2021), https://doi.org/10.1002/GAMM.202100003/FORMAT/PDF.
[39] C. Fragassa, M. Babic, C.P. Bergmann, G. Minak, Predicting the Tensile Behaviour of Cast Alloys by a Pattern Recognition Analysis on Experimental Data, (2019).
[40] I. Santos, J. Nieves, Y.K. Penya, P.G. Bringas, Machine-learning-based mechanical properties prediction in foundry production Machine-learning-based Mechanical Properties Prediction in Foundry Production, (2009).
[41] S. Pattanayak, S. Dey, S. Chatterjee, S. Ghosh, Computational intelligence based designing of microalloyed pipeline steel, Comput. Mater. Sci. 104 (2015) 60–68, https://doi.org/10.1016/j.commatsci.2015.03.029.
[42] H. Wang, H. Luo, Z. Han, Q. Zhong, Investigation of damage identification of 16Mn steel based on artificial neural networks and data fusion techniques in tensile test, Lect. Notes Comput. Sci. (Including Subser. Lect. Notes Artif. Intell. Lect. Notes Bioinformatics) 5678 (2009) 696–703, https://doi.org/10.1007/978-3-642-03348-3_73/COVER.
[43] X. Li, A brief review: acoustic emission method for tool wear monitoring during turning, Int. J. Mach. Tools Manuf. 42 (2002) 157–165, https://doi.org/10.1016/S0890-6955(01)00108-0.
[44] D. Bianchi, E. Mayrhofer, M. Gröschl, G. Betz, A. Vernes, Wavelet packet transform for detection of single events in acoustic emission signals, Mech. Syst. Signal Process. 64–65 (2015) 441–451, https://doi.org/10.1016/j.ymssp.2015.04.014.
[45] N.E. Huang, Z. Shen, S.R. Long, M.C. Wu, H.H. Shih, Q. Zheng, N.-C. Yen, C.C. Tung, H.H. Liu, The empirical mode decomposition and the Hilbert spectrum for nonlinear and non-stationary time series analysis, Proc. r. Soc. London. Ser. A Math. Phys. Eng. Sci. 454 (1998) 903–995.
[46] Z. Wu, N.E. Huang, Ensemble empirical mode decomposition: a noise-assisted data analysis method, Adv. Adapt. Data Anal. 1 (2011) 1–41, https://doi.org/10.1142/S1793536909000047.
[47] K. Dragomiretskiy, D. Zosso, Variational mode decomposition, IEEE Trans. Signal Process. 62 (2014) 531–544, https://doi.org/10.1109/TSP.2013.2288675.
[48] X. Zhao, P. Wu, X. Yin, A quadratic penalty item optimal variational mode decomposition method based on single-objective salp swarm algorithm, Mech. Syst. Signal Process. 138 (2020) 106567, https://doi.org/10.1016/J.YMSSP.2019.106567.
[49] Y. Zhou, Z. Zhu, A hybrid method for noise suppression using variational mode decomposition and singular spectrum analysis, J. Appl. Geophys. 161 (2019) 105–115, https://doi.org/10.1016/J.JAPPGEO.2018.10.025.
[50] Y. Zhou, G. Wu, Unsupervised machine learning for waveform extraction in microseismic denoising, J. Appl. Geophys. 173 (2020) 103879, https://doi.org/10.1016/J.JAPPGEO.2019.103879.
[51] S. Sud, Combined variational mode decomposition and singular spectral analysis for blind source separation in low signal-to-noise ratio environments, Conf. Proc. - IEEE Southeastcon. (2021), https://doi.org/10.1109/SOUTHEASTCON45413.2021.9401937.
[52] D.S. Broomhead, G.P. King, On the qualitative analysis of experimental dynamic systems, Phys. D Nonlinear Phenom. 20 (1986) 217–236.
[53] Y.J. Natarajan, D. Subramaniam Nachimuthu, New SVM kernel soft computing models for wind speed prediction in renewable energy applications, Soft Comput. 24 (2020) 11441–11458, https://doi.org/10.1007/S00500-019-04608-W/TABLES/5.
[54] L. Xiang, J. Li, A. Hu, Y. Zhang, Deterministic and probabilistic multi-step forecasting for short-term wind speed based on secondary decomposition and a deep learning method, Energy Convers. Manag. 220 (2020) 113098.
[55] L. Xu, S. Chatterton, P. Pennacchi, Rolling element bearing diagnosis based on singular value decomposition and composite squared envelope spectrum, Mech. Syst. Signal Process. 148 (2021) 107174, https://doi.org/10.1016/J.YMSSP.2020.107174.
[56] J. Fu, F. Cai, Y. Guo, H. Liu, W. Niu, An improved VMD-based denoising method for time domain load signal combining wavelet with singular spectrum analysis, Math. Probl. Eng. 2020 (2020), https://doi.org/10.1155/2020/1485937.
[57] S. Chen, K. Guo, P. Zeng, X. Lv, Z. Jia, J. Yang, A load classification framework based on VMD and singular value energy difference spectrum, IEEE Int. Conf. Energy Internet (2019) 398–402.
[58] N. Golyandina, V. Nekrutkin, A.A. Zhigljavsky, Analysis of time series structure: SSA and related techniques, CRC Press, 2001.
[59] B.W. Wah, T. Wang, Y. Shang, Z. Wu, Improving the performance of weighted Lagrange-multiplier methods for nonlinear constrained optimization, Inf. Sci. (NY) 124 (2000) 241–272, https://doi.org/10.1016/S0020-0255(99)00081-X.
[60] S. Sud, Blind, non-stationary source separation using variational mode decomposition with mode culling, signal process, accessed November 15, 2022, An Int. J. 13 (2020) 11–20, https://www.slideshare.net/CSCJournals/blind-nonstationary-source-separation-using-variational-mode-decomposition-with-mode-culling.
[61] K. Horváth, D. Drozdenko, K. Máthis, J. Bohlen, P. Dobroň, Deformation behavior and acoustic emission response on uniaxial compression of extruded rectangular profile of MgZnZr alloy, J. Alloys Compd. 680 (2016) 623–632, https://doi.org/10.1016/J.JALLCOM.2016.03.310.

[62] Z.K. Peng, M.R. Jackson, J.A. Rongong, F.L. Chu, R.M. Parkin, On the energy leakage of discrete wavelet transform, Mech. Syst. Signal Process. 23 (2009) 330–343.
[63] D. Ozevin, MEMS acoustic emission sensors, Appl. Sci. 10 (2020) 8966, https://doi.org/10.3390/app10248966.
[64] L. Toubal, H. Chaabouni, P. Bocher, C. Jianqiang, Monitoring fracture of high-strength steel under tensile and constant loading using acoustic emission analysis, Eng. Fail. Anal. 108 (2020) 104260, https://doi.org/10.1016/j.engfailanal.2019.104260.
[65] A. Deng, L. Zhao, Y. Bao, Acoustic emission recognition using fuzzy entropy, Proc. - 2009 IEEE Int. Conf. Intell. Comput. Intell. Syst. ICIS 2009. 4 (2009) 75–79. https://doi.org/10.1109/ICICISYS.2009.5357744.
[66] Y. Wei, Y. Yang, M. Xu, W. Huang, Intelligent fault diagnosis of planetary gearbox based on refined composite hierarchical fuzzy entropy and random forest, ISA Trans. 109 (2021) 340–351, https://doi.org/10.1016/J.ISATRA.2020.10.028.
[67] D.R. Askeland, P.P. Fulay, Essential of materials science and Engineering (2nd end), New York, USA, 2010.
[68] Q. Tian, H. Luo, R. Yi, X. Fan, Y. Ma, D. Shi, J. Gao, Study of micro-plastic deformation in pure iron before macro-yielding using acoustic emission, electron backscattered diffraction and transmission electron microscopy, Mater. Sci. Eng. A. 771 (2020) 138645, https://doi.org/10.1016/J.MSEA.2019.138645.
[69] A. Vinogradov, A.V. Danyuk, D.L. Merson, I.S. Yasnikov, Probing elementary dislocation mechanisms of local plastic deformation by the advanced acoustic emission technique, Scr. Mater. 151 (2018) 53–56, https://doi.org/10.1016/j.scriptamat.2018.03.036.
[70] G.D. Fan, M.Y. Zheng, X.S. Hu, K. Wu, W.M. Gan, H.G. Brokmeier, Internal friction and microplastic deformation behavior of pure magnesium processed by equal channel angular pressing, Mater. Sci. Eng. A. 561 (2013) 100–108, https://doi.org/10.1016/j.msea.2012.10.083.
[71] A1035/A1035M Standard Specification for Deformed and Plain, Low-Carbon, Chromium, Steel Bars for Concrete Reinforcement, 2023.
[72] F. Wuttke, H. Lyu, A.S. Sattari, Z.H. Rizvi, Wave based damage detection in solid structures using artificial neural networks, (2021). http://arxiv.org/abs/2103.16339 (accessed April 30, 2021).
[73] V. Soltangharaei, R. Anay, L. Assi, M. Bayat, J.R. Rose, P. Ziehl, Analyzing acoustic emission data to identify cracking modes in cement paste using an artificial neural network, Constr. Build. Mater. (2020) 121047, https://doi.org/10.1016/j.conbuildmat.2020.121047.
[74] B. Chen, Y. Wang, Z. Yan, Use of acoustic emission and pattern recognition for crack detection of a large carbide anvil, Sensors (Switzerland). 18 (2018), https://doi.org/10.3390/s18020386.
[75] B. Muruganatham, M.A. Sanjith, B. Krishnakumar, S.A.V. Satya Murty, Roller element bearing fault diagnosis using singular spectrum analysis, Mech. Syst. Signal Process. 35 (2013) 150–166, https://doi.org/10.1016/J.YMSSP.2012.08.019.
[76] S.O. Sajedi, X. Liang, A data-driven framework for near real-time and robust damage diagnosis of building structures, Struct. Control Heal. Monit. 27 (2020), https://doi.org/10.1002/stc.2488.
[77] M. Azimi, G. Pekcan, Structural health monitoring using extremely compressed data through deep learning, Comput. Civ. Infrastruct. Eng. 35 (2020) 597–614, https://doi.org/10.1111/mice.12517.
[78] G. Ciaburro, G. Iannace, Machine-learning-based methods for acoustic emission testing: a review, Appl. Sci. 2022, Vol. 12, Page 10476. 12 (2022) 10476. https://doi.org/10.3390/APP122010476.
[79] Z. Chang, Z. Wan, Y. Xu, E. Schlangen, B. Šavija, Convolutional neural network for predicting crack pattern and stress-crack width curve of air-void structure in 3D printed concrete, Eng. Fract. Mech. 271 (2022) 108624, https://doi.org/10.1016/J.ENGFRACMECH.2022.108624.